Stillinger-Weber potential for the II-VI elements Zn-Cd-Hg-S-Se-Te

X. W. Zhou,[1,*] D. K. Ward,[2] J. E. Martin,[3] F. B. van Swol,[4] J. L. Cruz-Campa,[5] and D. Zubia[6]
[1]*Mechanics of Materials Department, Sandia National Laboratories, Livermore, California 94550, USA*
[2]*Radiation and Nuclear Detection Materials and Analysis Department, Sandia National Laboratories, Livermore, California 94550, USA*
[3]*Nanoscale Sciences Department, Sandia National Laboratories, Albuquerque, New Mexico 87185, USA*
[4]*Computational Materials and Data Science Department, Sandia National Laboratories, Albuquerque, New Mexico 87185, USA*
[5]*MEMS Technologies Department, Sandia National Laboratories, Albuquerque, New Mexico 87185, USA*
[6]*Department of Electrical Engineering, University of Texas at El Paso, El Paso, Texas 79968, USA*
(Received 30 May 2013; published 9 August 2013; corrected 13 November 2013)

Bulk and multilayered thin film crystals of II-VI semiconductor compounds are the leading materials for infrared sensing, γ-ray detection, photovoltaics, and quantum dot lighting applications. The key to achieving high performance for these applications is reducing crystallographic defects. Unfortunately, past efforts to improve these materials have been prolonged due to a lack of understanding with regards to defect formation and evolution mechanisms. To enable high-fidelity and high-efficiency atomistic simulations of defect mechanisms, this paper develops a Stillinger-Weber interatomic potential database for semiconductor compounds composed of the major II-VI elements Zn, Cd, Hg, S, Se, and Te. The potential's fidelity is achieved by optimizing all the pertinent model parameters, by imposing reasonable energy trends to correctly capture the transformation between elemental, solid solution, and compound phases, and by capturing exactly the experimental cohesive energies, lattice constants, and bulk moduli of all binary compounds. Verification tests indicate that our model correctly predicts crystalline growth of all binary compounds during molecular dynamics simulations of vapor deposition. Two stringent cases convincingly show that our potential is applicable for a variety of compound configurations involving all the six elements considered here. In the first case, we demonstrate a successful molecular dynamics simulation of crystalline growth of an alloyed $(Cd_{0.28}Zn_{0.68}Hg_{0.04})$ $(Te_{0.20}Se_{0.18}S_{0.62})$ compound on a ZnS substrate. In the second case, we demonstrate the predictive power of our model on defects, such as misfit dislocations, stacking faults, and subgrain nucleation, using a complex growth simulation of ZnS/CdSe/HgTe multilayers that also contain all the six elements considered here. Using CdTe as a case study, a comprehensive comparison of our potential with literature potentials is also made. Finally, we also propose unique insights for improving the Stillinger-Weber potential in future developments.

DOI: 10.1103/PhysRevB.88.085309 PACS number(s): 34.20.Cf, 83.10.Rs, 81.05.Dz, 68.65.Ac

I. INTRODUCTION

Bulk and multilayered thin film crystals of II-VI compounds composed of Zn, Cd, Hg, S, Se, and Te are important semiconductor materials. For instance, $Hg_{1-x}Cd_xTe$ has been the leading material for infrared sensing;[1,2] $Cd_{1-x}Zn_xTe$ (CZT) has long been the dominant semiconductor for radiation-detection;[3–6] CdTe/CdS solar cells are currently the lowest cost photovoltaic technology;[7] and CdTe/CdS quantum dots are being actively explored for optoelectronic applications.[8] The quality and performance of these materials are critically limited by various crystallographic defects. In particular, reducing the misfit and threading dislocation density is essential for improving efficiency of $Hg_{1-x}Cd_xTe$ infrared detectors,[1,2] CdTe/CdS solar cells,[9] and CdTe/CdS quantum dots.[8] Controlling dislocation network structures, on the other hand, can help reduce property nonuniformity of radiation detecting CZT crystals[3,10,11] that contributes to both high cost and poor performance. Unfortunately, these property-limiting defects are thermodynamically stable, and have been difficult to remove and control. Classical molecular dynamics (MD) simulations can reveal the defect formation and evolution mechanisms without *a priori* assumptions about these defects and therefore help guide defect reduction efforts. However, such simulations require an interatomic potential with a sufficient fidelity to allow crystalline growth vapor deposition simulations.

In recent years, the present authors have been involved in developing an analytical bond order potential (BOP) for Cd-Zn-Te systems.[12,13] Bond order potential[14–18] and, to a smaller extent, the Tersoff potential[19] (which is essentially a simpler form of BOP), have many advantages. The most important is that they can capture property trends of a variety of structures and compositions. By capturing energy trends of different compositions, this type of BOP enables chemical vapor deposition simulations.[20] In other words, these simulations can capture the growth of stoichiometric compound crystal (i.e. total II-type atoms equals the total VI-type atoms) from nonstoichiometric vapor fluxes because atoms of any excess species would predominantly evaporate from growth surfaces due to correctly predicted higher energies. However, extending BOP to include six elements is not a trivial effort. Stillinger-Weber (SW) potentials[21] use an energy penalty for nontetrahedral bond angles to ensure the tetrahedral structure, such as diamond-cubic (dc), zinc-blende (zb), or wurtzite (wz) crystals, as the lowest energy structures. Under stoichiometric conditions, all II-VI compounds exhibit either a zb or a wz structure. If a sufficient energy penalty is applied to ensure that only zb or wz occurs during growth simulations under stoichiometric conditions, as observed in experiments, then the SW potential may realistically reveal the defect formation mechanisms. This assumes that the lattice constants, cohesive energies, and elastic constants of these zb

or wz compound phases are well captured. For instance, the formation of misfit dislocations between different compound layers is dictated by the lattice and elastic constants of the layers.

Due to its simplicity, the SW potentials are currently the most widely used (∼2500 citations) semiconductor interatomic potentials. Despite wide applications, a satisfactory SW potential database that includes sufficient II-VI elements for a study of any of the four systems cited above ($Hg_{1-x}Cd_xTe$ infrared sensing, $Cd_{1-x}Zn_xTe$ radiation detection, CdTe/CdS solar cell, and CdTe/CdSe quantum dot) has not been developed. While efforts have been made to construct multielement SW potentials for Ga-In-As-Se-Te,[22] Al-Ga-In-P-As-Sb,[23] and Cd-Te-Zn-As-Si[24] systems, these potentials can probably be further improved as their parameters have not been fully optimized (i.e. many parameters are selected and fixed during parameterization).[22,24] Furthermore, some of these potentials do not provide a complete set of parameters (in particular, only parameters between different species ij are given, but parameters between the same species ii or jj are missing).[23] The potential developed recently by Zhang *et al.*[24] does include Cd, Zn, and Te needed for studying $Cd_{1-x}Zn_xTe$ radiation-detection crystals. The primary parameters of this potential are directly taken from some well-accepted SW potentials for Cd-Te (Ref. 25), Zn-Te (Ref. 22), As (Ref. 22), and Si (Ref. 21) systems, and the remaining parameters are fitted to density functional theory (DFT) calculations of distortion energies. Interestingly, the authors demonstrated that the arsenic-related portion of the potential is not satisfactory, and the ZnTe/Si structure predicted by the potential is overly defective.[24] High-fidelity atomistic simulations of multielement semiconductor compounds, therefore, demand development of new SW potential parameterization methods that overcome these problems. The objective of the present work is to develop a Zn-Cd-Hg-S-Se-Te SW potential including all II and VI elements except oxygen and polonium. Differing from previous work, our potential is parameterized based upon a conscientious understanding of the SW potential so that the parameters that may impact the properties are all optimized. In particular, we ensure that our potential reproduces the experimental lattice constants, cohesive energies, and elastic constants of all binary compounds and at the same time possesses appropriate energy trends so that it correctly predicts the formation of stoichiometric compounds under stoichiometric conditions. We have verified that our potential correctly predicts the crystalline growth of all nine compounds during molecular dynamics simulations of vapor deposition. It should be noted that vapor deposition simulations are not always tested in potential development but are extremely important because they sample a variety of off-lattice configurations statistically formed on the growth surface that are unknown *a priori*. If any of these configurations have (incorrectly) a lower energy than the equilibrium growth crystal, phase transformation is likely triggered, resulting in an amorphous structure that provides no useful information. Here, we present two extremely challenging cases. In the first case, we demonstrate a successful MD simulation of crystalline growth of an alloyed $(Cd_{0.28}Zn_{0.68}Hg_{0.04})(Te_{0.20}Se_{0.18}S_{0.62})$ compound on a ZnS substrate. This can convincingly verify the applicability of our potential to any stoichiometric configurations involving up to all the six elements considered here. In the second case, we will demonstrate the predictive power of our model on defect formation using a complex case of MD vapor deposition simulation of HgTe/CdSe/ZnS compound multilayers.

II. POTENTIAL FORMAT

Rewritten from the original SW potential,[21] the total energy of a system of N atoms can be expressed as

$$E = \frac{1}{2}\sum_{i=1}^{N}\sum_{j=i_1}^{i_N}\left[V_{IJ}^{R}(r_{ij}) - V_{IJ}^{A}(r_{ij}) + u_{IJ}(r_{ij}) \times \sum_{\substack{k=i_1\\k\neq j}}^{i_N} u_{IK}(r_{ik})\left(\cos\theta_{jik} + \frac{1}{3}\right)^2\right], \quad (1)$$

where $i_1, i_2, \ldots, i_N$ is a list of neighbors of atom i, θ_{jik} is the bond angle formed by atoms j and k at the site of atom i, $V_{IJ}^{R}(r_{ij})$ and $V_{IJ}^{A}(r_{ij})$ are, respectively, pairwise repulsive and attractive functions, $u_{IJ}(r_{ij})$ is another pair function, and subscripts ij and IJ indicate, respectively, the pair of atoms and the species of the pair of atoms. Here, the functions $V_{IJ}^{R}(r_{ij})$, $V_{IJ}^{A}(r_{ij})$, and $u_{IJ}(r_{ij})$ are expressed as

$$V_{IJ}^{R}(r) = A_{IJ}\varepsilon_{IJ}B_{IJ}\left(\frac{\sigma_{IJ}}{r}\right)^{p}\exp\left(\frac{\sigma_{IJ}}{r - a_{IJ}\sigma_{IJ}}\right), \quad (2)$$

$$V_{IJ}^{A}(r) = A_{IJ}\varepsilon_{IJ}\left(\frac{\sigma_{IJ}}{r}\right)^{q}\exp\left(\frac{\sigma_{IJ}}{r - a_{IJ}\sigma_{IJ}}\right), \quad (3)$$

and

$$u_{IJ}(r) = \sqrt{\lambda_{IJ}\varepsilon_{IJ}}\exp\left(\frac{\gamma_{IJ}\sigma_{IJ}}{r - a_{IJ}\sigma_{IJ}}\right), \quad (4)$$

where ε, σ, a, λ, γ, A, and B are seven pair-dependent parameters, and p and q are not fitted but are taken as the values of 4 and 0, respectively. Note that $a\sigma$ represents the interaction range of the potential so that when $r \geqslant a\sigma$, pair functions $V^R(r)$, $V^A(r)$, and $u_{IJ}(r)$ all vanish. Stillinger-Weber potentials have some important features that are considered in our parameterization. For convenience, these features are discussed in the following separate subsections.

A. Nearest-neighbor model for tetrahedral crystals

Equation (1) is essentially a summation of a pair term $\phi_{IJ}(r_{ij}) = V_{IJ}^{R}(r_{ij}) - V_{IJ}^{A}(r_{ij})$ and a three-body term $u_{IJ}(r_{ij})u_{IK}(r_{ik})(\cos\theta_{jik} + \frac{1}{3})^2$. This is exactly the same as the Tersoff potential,[19] and hence SW and Tersoff potentials can be coded using the same subroutine in molecular dynamics programs. In SW potentials, however, the pair function $\phi_{IJ}(r_{ij})$ includes both attractive $-V_{IJ}^{A}(r_{ij})$ and repulsive $V_{IJ}^{R}(r_{ij})$ energies, and the three-body term $u_{IJ}(r_{ij})u_{IK}(r_{ik})(\cos\theta_{jik} + \frac{1}{3})^2$ is essentially a positive energy penalizing nontetrahedral bond angles (i.e. $\cos\theta_{jik} \neq -1/3$). In the Tersoff potential, on the other hand, the pair function represents a repulsive energy, and the three-body term is a bond order modified negative (attractive) energy. It can be seen that, when the SW potential is used as a nearest-neighbor model for tetrahedral

structures where $\cos\theta_{jik}$ always equals $-1/3$, these structures would naturally possess the lowest energy compared to other structures as long as the prefactor functions $u_{IJ}(r_{ij})$ or $u_{IK}(r_{ik})$ are sufficiently large. This can always be achieved by using a large scaling parameter value for λ_{IJ} as seen from Eq. (4). This makes the model and the parameterization extremely simple. In contrast, a large number of structures must be specifically considered during Tersoff potential parameterization in order to ensure the lowest energy for the dc, zb, or wz structure. This is not a trivial task as it is not always clear which target structures should be included in the training set.

Stillinger-Weber potentials can also be employed while including more than just the nearest-neighbors and for nontetrahedral structures. In these cases, however, SW potentials are often not significantly simpler than the Tersoff potentials. As a result, Tersoff potentials often become the preferred choice as they are constructed based upon the bond order concept derived from quantum mechanical theories and can better capture property trends of a large number of target structures. However, as will be demonstrated below, SW potentials can be easily parameterized to produce the lowest energy for simple nontetrahedral structures for elements (e.g., face centered cubic). This property can be utilized to construct SW alloy models that are simpler than the Tersoff counterparts but still exhibit reasonable energy trends when the elemental systems have simple crystal structures.

B. Scalability

For any elemental system described by the SW potential, the lattice constant always scales with the parameter σ, and the cohesive energy always scales with the parameter ε. If only σ and ε are changed, the order of cohesive energies of different phases remains unchanged because these cohesive energies all scale with ε. This means that σ and ε can be rescaled to match the lattice constant and the cohesive energy of the lowest energy phase of any material without reparameterization. For example, Si SW potential has been well developed.[21] As Si has a dc crystal structure, one can then create a SW potential for any dc element with arbitrary lattice constant and cohesive energy. This is also applicable to the parameters between different species in a binary compound. This simple scaling, however, does not result in optimized elastic constants. It is still expected to give relatively reasonable elastic constants because, experimentally, bulk modulus B approximately scales with cohesive energy E_c through $B \propto E_c/\Omega$ (Ref. 26) where Ω is atomic volume.

C. Property-parameter correspondence

When a tetrahedral structure is subjected to a hydrostatic strain, the bond angles remain tetrahedral, and the angular term of Eq. (1) vanishes. In such a case, the SW potential reduces to a pair potential model. Equations (2) and (3) indicate that the pair component of the SW potential essentially has four parameters $p_1 = \varepsilon A$, $p_2 = B$, $p_3 = \sigma$, and $p_4 = a\sigma$. However, not all these parameters are completely independent. For instance, repulsive interaction should always be harder than the attractive interaction when atoms approach the equilibrium bond length, and the cutoff distance $p_4 = a\sigma$ needs to be below the second-nearest-neighbor distance for the SW potential to be a nearest-neighbor model. The hardness and cutoff constraints effectively reduce the formal number of free parameters to three or below. For tetrahedral structures, these free parameters allow fitting of the three fundamental material properties: lattice constant, cohesive energy, and bulk modulus. However, we have found that, for the nearest-neighbor models of the elemental fcc structures, these parameters can only fit lattice constant and cohesive energy, whereas the bulk modulus range that can be fitted is significantly larger than that of real materials.[27] This is because, in SW potentials, the second derivative of the bond energy at the equilibrium bond length increases with decreasing cutoff distance so that there exists a minimum second derivative for the nearest-neighbor models, which in turn leads to a minimum bulk modulus.

Cubic crystals have three independent elastic constants, for example, the bulk modulus B and two additional shear moduli C' and C_{44}. It can be shown that, when the parameters for the pair energy are given, the function value $u(r)$ in the angular term [see Eq. (4)] can be used to further fit a shear modulus (e.g., C') of a cubic structure.[28,29] As will be further discussed below, however, this refinement is subject to the constraint that $u(r)$ must be sufficiently large to ensure the lowest energy for the equilibrium tetrahedral structures.

D. Cutoff

Unlike the independent treatment of the cutoff for many other potentials, the SW potential functions smoothly approach zero at the interaction range $r = a\sigma$. This is sometimes an advantage over other potentials; for example, it results in better thermal conductivity calculations.[30] However, it should also be noted that the value of the SW potential becomes negligibly small way before the distance reaches the theoretical interaction range. To examine this, a SW pair function $\phi(r) = V^R(r) - V^A(r) = [B(\frac{\sigma}{r})^4 - 1]\exp(\frac{\sigma}{r-a\sigma})$ is plotted in Fig. 1 as a function of r using typical parameters $B = 0.72$, $\sigma = 2.1$, and $a = 1.6$ (setting the multiplicative factor $A\varepsilon = 1$). It can be seen that, while the theoretical interaction distance is 3.36 Å, the potential virtually drops to negligible values at a distance near 3.1 Å. This feature allows SW potential to be designed at

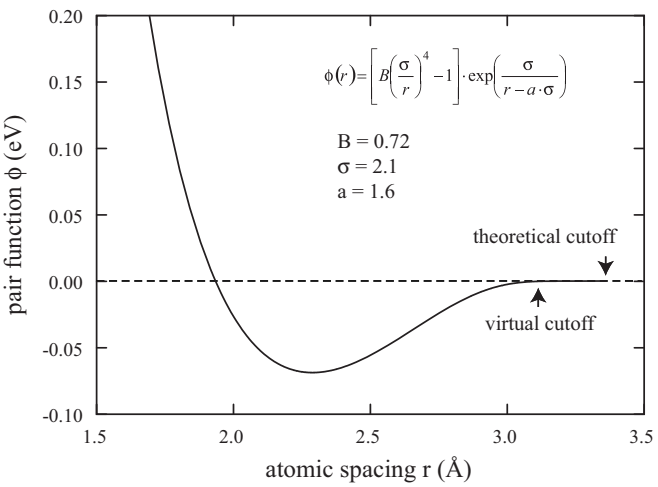

FIG. 1. Cutoff of a typical SW potential pair function.

$a\sigma$ above the second-nearest-neighbor distance, whereas the potential can still be considered as a nearest-neighbor model. It can also be used to accelerate the simulations by using a virtual cutoff distance substantially shorter than $a\sigma$ for finding the neighbor list during MD simulations so that the neighbors that make negligible contributions to energies are not included in computations.

III. PARAMETERIZATION OF POTENTIAL

The goal of this work is to develop an atomistic model for studying compounds under stoichiometric conditions. The challenge is that we are not simply dealing with a known equilibrium structure, but rather a structure predicted from MD simulations of vapor deposition involving six different elements. As a variety of off-lattice configurations with different compositions are nucleated on the surface during random adatom condensation, it is extremely important to ensure that these configurations all correctly evolve towards the growth compound crystal. This can be achieved by capturing correctly the energy trends between nonstoichiometric elements, nonstoichiometric solid solutions, and stoichiometric compounds. Here, nonstoichiometric solid solutions refer to alloys composed of only anion or cation elements. In reality, these alloyed systems likely inherit the crystal structure of their constituent element (e.g., Cd_xZn_{1-x} alloys likely have the same crystal structure as Zn either because x is small or because Cd also has the same crystal structure as Zn).

The room temperature lowest energy elemental phases are hexagonal close packed (hcp) for Cd and Zn, hexagonal (commonly referred to as A8) for Te and Se, orthorhombic (orth) for S, and liquid for Hg (Ref. 31). Stillinger-Weber potentials approximate quite well hcp as the lowest energy phase when it captures the fcc phase because these two phases have the same nearest-neighbor bond length and bond angles. This means that fcc can be used as the target structure for Cd and Zn. A SW potential can also capture the liquid Hg if the predicted melting point is below room temperature. Hence, fcc with a sufficiently low melting point (or cohesive energy) can also be used to approximate Hg. Stillinger-Weber potentials cannot easily capture A8 and orth-S structures as the lowest energy phases (similar to many other potentials), so an approximation is made. It should be noted that in order for a stoichiometric compound to incorrectly separate into elemental domains during simulation, these domains are necessarily the lowest energy elemental phases in the model. In other words, if we specify an energy difference between a compound and the lowest energy elemental phases in the model equal to the energy difference between a compound and the lowest energy elemental phases in reality, the elemental phases will naturally not form in stoichiometric simulations as all possible elemental structures will have unfavorable energies. Since elemental domains do not form, details of elemental structures do not affect the results. In this sense, only a representative lowest energy elemental structure (with the same density as the realistic structure) is needed to ensure the correct transformation (energy difference) between compounds and elements. It is with this recognition that we also use fcc to approximate A8-Te, A8-Se [A8 structure is essentially a "strained" fcc structure that has smaller (111) spacing (may have additional internal relaxation)], and orth-S. Note that the common literature SW potentials use either fcc (Refs. 32 and 33) or even dc (Ref. 25) structure to approximate elemental systems.

Using the definition described above, a nonstoichiometric binary system is composed of either two cation elements or two anion elements. For all the nonstoichiometric binary systems encountered here, TeSe forms solid solutions, CdZn separates into Cd-rich and Zn-rich solutions, and TeS separates into Te and S solids. CdHg, ZnHg, and SeS are more complicated as they form some intermediate solid solutions. As has been discussed above, our goal is to study the growth of stoichiometric compounds under stoichiometric conditions where no nonstoichiometric domains form. Regardless of what the real lowest energy phase is, we can always use a representative structure to represent the lowest energy phase of a nonstoichiometric system so that, when the energy of this lowest energy phase is sufficiently high with respect to the stoichiometric compound, the formation of the nonstoichiometric phases will be correctly prohibited during growth of the stoichiometric compound. Because nonstoichiometric structures do not form, details of structures do not really affect the results. It is based on this important recognition that we use zb crystal as the representative structure for all nonstoichiometric binary systems.

For the stoichiometric binary compounds encountered here, CdTe, CdSe, ZnTe, HgTe, ZnSe, ZnS, HgSe, and HgS have a zb structure, and CdS has a wz structure (although the zb form is also experimentally observed). The SW potential does not distinguish zb and wz structures energetically (they both have the same nearest-neighbor distances and nearest-neighbor bond angles). As a result, all these compounds can be captured by the zb structure. The consequence of the SW potentials not distinguishing between zb and wz structures can be evaluated through additional insights. First, *ab initio* calculations have been used to determine the energy difference between wz and zb structures as $\Delta E = E_{wz} - E_{zb} = -0.001$, 0.003, 0.005, and 0.006 eV/atom for CdS, ZnS, ZnSe, and ZnTe, respectively.[34] Furthermore, ΔE approximately equals 0.000, 0.006, 0.006, 0.009, and 0.017 eV/atom for CdSe, HgS, HgSe, CdTe, and HgTe, respectively, based on a ΔE vs Pauling's electronegativity relationship.[34] It can be seen that, except for HgTe, the absolute values of these energy differences are rather small, and as a result, the SW approximation here may be quite good. For instance, CdTe has a wz-zb energy difference at the high end (0.009 eV/atom), but CdTe has only a low stacking fault energy around 10 mJ/m^2.[35,36] Secondly, even though SW potentials prescribe equal energies for wz and zb structures, they prescribe slightly more negative Gibbs free energies for the zb (or similarly the face centered cubic) structure than for the wz (or similarly the hexagonal closely packed) structure.[37,38] This is in line with HgTe where the zb structure is more stable. Note that the 0.017 eV/atom wz-zb energy difference of HgTe is relatively large compared to other compound systems considered here. For reference, aluminum is known to have a high stacking fault energy, and aluminum has a considerably higher hcp-fcc energy difference of 0.05 eV/atom.[39,40]

TABLE I. With universal parameters $\lambda = 32.5$ and $\gamma = 1.2$ for all pairs, a complete list of all other parameters of the Zn-Cd-Hg-S-Se-Te SW potential (energy in unit eV and length in unit Å).

Pair ij	ε	σ	a	A	B
CdCd	1.182358	2.663951	1.527956	7.9170	0.767446
CdTe	1.385284	2.352141	1.810919	7.0496	0.886125
CdZn	0.690818	2.238699	1.812616	7.0496	1.010632
CdSe	1.352371	2.045165	1.953387	7.0496	1.116149
CdHg	0.488123	2.432694	1.677987	7.0496	0.625100
CdS	1.300376	1.804151	2.124568	7.0496	1.540087
TeTe	1.849775	2.905254	1.594353	7.9170	0.730728
TeZn	1.546239	2.056363	1.907922	7.0496	1.255846
TeSe	1.295053	2.231716	1.809645	7.0496	1.005396
TeHg	1.204715	2.135591	1.892491	7.0496	1.445180
TeS	1.450015	2.297301	1.726905	7.0496	0.779469
ZnZn	1.392961	2.367650	1.525521	7.9170	0.767628
ZnSe	1.691181	2.028827	1.836907	7.0496	0.951093
ZnHg	0.495162	2.239186	1.761363	7.0496	0.746117
ZnS	2.208390	2.323783	1.589241	7.0496	0.464318
SeSe	2.400781	2.789002	1.544925	7.9170	0.767213
SeHg	1.299758	2.113406	1.831821	7.0496	1.150200
SeS	1.307592	2.229392	1.747782	7.0496	0.693232
HgHg	1.272807	2.699097	1.498503	7.9170	1.211532
HgS	1.531211	2.025045	1.833708	7.0496	1.184541
SS	2.434871	2.423171	1.711097	7.9170	1.049688

Literature SW potentials typically do not fully optimize all parameters. For example, parameters ε, σ, a, γ, and λ are selected in Refs. 22,25, and 41, parameters A, B, a, γ, and λ are selected in Ref. 42, and the scalability rule is used to convert parameters for different materials without parameterization in Ref. 43. We note that A is not an independent parameter as it can be combined with ε in Eqs. (2) and (3), and this consolidation does not affect Eq. (4) as long as we replace λ with λ/A, so we fix A ($A = 7.9170$ is used for elemental systems and $A = 7.0496$ is used for binary systems, purely due to historically reasons) without fitting it. As shown above, γ and λ for the three-body term only affect the shear modulus (C' or C_{44}) but they must be constrained to give the lowest energy for the tetrahedral structure for the compounds. Here, we fix $\gamma = 1.2$ and $\lambda = 32.5$ as is commonly done in the literature[22,23,41,42] because these choices of γ and λ values easily ensure the lowest energy for the tetrahedral structure.

Experimental cohesive energies[39] and atomic volumes (lattice constants or material density)[31] are available for all the six elements (Zn, Cd, Hg, S, Se, and Te). Experimental cohesive energies,[39] lattice constants,[31] and bulk moduli[44–48] are available for all the nine zb structures (CdTe, CdSe, ZnTe, HgTe, ZnSe, ZnS, HgSe, HgS, and CdS). These experimental properties are used directly as the target values for the parameterization. Experimental energies and lattice constants are not available for the six alloyed systems (TeSe, TeS, CdZn, CdHg, ZnHg, and SeS) and these properties are therefore estimated. In particular, the lattice constants and cohesive energies of the alloyed systems are taken, respectively, as arithmetic and geometric means of the corresponding values for the zb compounds (containing the relevant elements in the alloys). Additionally, the energies are constrained to give a positive heat of mixing to ensure that these alloyed structures do not occur during simulations. Again, detailed lattice constants and cohesive energies of these alloys are not particularly important because these alloyed phases do not occur. Nonetheless, the treatment is reasonable and in line with a common alloy mixing rule in literature where length and energy parameters are taken as arithmetic and geometric means of the corresponding elemental parameters.[49] The estimated energies and lattice constants of these alloyed systems are then used as the target values. Optimization is done to fit all the target properties determined as described above with the constraints that cutoff distances only include the nearest neighbors, and the targeted structures have the lowest energies relative to any other configuration of the same materials. The resulting fitted parameters are listed in Table I.

The parameters shown in Table I are obtained with the constraint of fixed γ and λ. As shown previously,[28,29] the parameters γ and λ for the three-body term affect the shear modulus (C' or C_{44}) through their combined effect on the angular function value $u(r_0)$ at the equilibrium bond length r_0, Eq. (4). To explore this further, we perform a second parameterization for all the zb compounds where γ and λ are not fixed but rather the value of $u(r_0)$, denoted as the parameter u_0, is optimized to capture the shear modulus C'. The values of r_0 and u_0 are listed in Table II.

One important notion about the SW potential is that, while the γ and λ parameters provided in Table I make a functional potential, users do not have to stick with these parameters. In an extreme limit, users can adjust γ and λ using the parameters u_0 and r_0 given in Table II. In particular, one can choose an appropriate value for λ and then solve γ from $u(r_0) = u_0$ (or solve λ from chosen γ). As an example, we have used this approach to create a set for λ and γ parameters for all the stoichiometric pairs at a selected value of $\lambda = 5.0$, and the results are included in Table II. The γ and λ parameters thus obtained capture the shear modulus C'. Obviously, such an approach does not always ensure the lowest energies for the desired tetrahedral structures as will be demonstrated below. If this occurs, users can always choose a value $u_0' > u_0$ such that the γ and λ parameters obtained from $u(r_0) = u_0'$ ensures the lowest energy for the tetrahedral structures. We believe

TABLE II. Parameters u_0 and r_0 and modified λ and γ for stoichiometric pairs. Here, $\lambda = 5.0$ is selected, and γ is obtained from $u(r_0) = u_0$.

Pair ij	CdTe	CdSe	CdS	TeZn	TeHg	ZnSe	ZnS	SeHg	HgS
r_0	2.80506	2.61973	2.52663	2.64181	2.79726	2.45475	2.34087	2.63445	2.53659
u_0	0.70496	0.70587	0.74281	1.00943	0.70874	1.00533	1.08445	0.62285	0.65118
λ	5.00000	5.00000	5.00000	5.00000	5.00000	5.00000	5.00000	5.00000	5.00000
γ	0.81456	0.87686	0.89310	0.63147	0.72373	0.66592	0.65159	0.82481	0.84069

TABLE III. Predicted energies per atom (eV) of selected structures for various materials. The first column of data is for the target structures. Numbers in bold highlight the lowest energies. Here, fcc: face centered cubic; hcp: hexagonal close packed; bcc: body centered cubic; sc: simple cubic; dc: diamond cubic; zb: zinc-blende; wz: wurtzite; B1: NaCl; B2: CsCl.

	Elements			
Material	fcc, hcp (target)	bcc	sc	dc
Zn	**−1.325**	−1.256	−1.118	−1.019
Cd	**−1.133**	−1.075	−0.958	−0.876
Hg	**−0.606**	−0.508	−0.435	−0.352
S	**−2.845**	−2.790	−2.660	−2.696
Se	**−2.414**	−2.310	−2.079	−1.930
Te	**−2.169**	−2.131	−1.983	−1.945
	Alloys			
	zb (target)	wz	B1	B2
CdZn	**−0.980**	−0.980	−0.836	−0.812
HgZn	**−0.780**	−0.780	−0.654	−0.640
CdHg	**−0.700**	−0.700	−0.612	−0.635
SeS	**−2.100**	−2.100	−1.762	−1.963
TeS	**−2.011**	−2.011	−1.813	−1.821
TeSe	**−1.830**	−1.830	−1.582	−1.695
	Compounds			
	zb (target)	wz	B1	B2
ZnS	**−3.080**	−3.080	−2.830	−2.561
ZnSe	**−2.694**	−2.694	−2.247	−2.085
ZnTe	**−2.364**	−2.364	−1.973	−1.815
CdS	**−2.763**	−2.763	−1.975	−1.901
CdSe	**−2.523**	−2.523	−1.939	−1.878
CdTe	**−2.178**	−2.178	−1.809	−1.776
HgS	**−2.004**	−2.004	−1.739	−1.853
HgSe	**−1.738**	−1.738	−1.500	−1.604
HgTe	**−1.554**	−1.554	−1.339	−1.424

that this additional user flexibility is easy enough to apply without significantly impacting the main characteristics of the potential. This can be important to utilize because it allows users to fine tune the potential for their specific applications (e.g., better shear modulus or melting temperature).

IV. CHARACTERISTIC PROPERTIES OF THE POTENTIAL

Molecular statics is used to relax structures and calculate energies for some selected phases of each material. The results are summarized in Table III where data for the lowest energy phases are reported in bold. With the notion that SW potential does not distinguish fcc and hcp structures (they also have close energies in DFT calculations as will be shown in Fig. 5 below), it can be seen from Table III that our potential correctly specifies the lowest energies for the target structures of each of the materials.

The relaxed configurations of the lowest energy structures of elements and compounds as well as their atomic volume, cohesive energy, and elastic constants are further compared with the available experimental values in Table IV. Table IV indicates that the potential exactly reproduces the experimental cohesive energies and atomic volumes for all elements and all compounds. Except for elements, the potential also reproduces the bulk modulus of all compounds exactly. It is important to note that the perfect matching of the experimental bulk modulus is the result of optimizing the interaction distance $a\sigma$, which has not been exploited in previous SW potential parameterizations.[22,23,41,42]

Similar calculations are also performed for all the compounds using modified parameters λ and γ, taken from Table II. The results obtained for the zb or wz compounds are included in Table IV. It can be seen that the adjusted parameters do not change lattice constants, cohesive energies, and bulk moduli of the zb or wz compounds, but will change their shear moduli C' and C_{44}. In fact, Table IV verifies that the modified λ and γ parameters reproduce the experimental elastic constant C' for all compounds exactly. It is also noted that the elastic constant C_{44} is not sensitive to the changes in the values of γ and λ, suggesting that the SW potential cannot effectively fit C_{44}. The predicted values of C_{44} listed in Table IV are seen to be significantly larger than the corresponding experimental values. This is because, unlike other elastic constants, C_{44} depends on internal relaxation of the crystal. The data shown in Table IV does not address this internal relaxation (this is indicated by an asterisk). As will be calculated below and also shown previously,[12,13] relaxed C_{44} is close to the experimental values.

Cohesive energies of selected phases of each compound are also calculated using the modified λ and γ parameters, and the results are shown in Table V. It can be seen that the reproduction of the experimental shear modulus C' by the modified parameters comes at the expense of generating the incorrect lowest energy structures for CdS, CdSe, and HgS. So when users attempt to modify λ and γ, the parameters should be chosen to first ensure the lowest energy for the equilibrium phase, and then the minimum $u(r_0)$ best captures the shear modulus C' in most cases.

V. VAPOR DEPOSITION SIMULATION

While not always tested in previous interatomic potential development, MD simulations of vapor deposition are important to verify for a number of reasons. First, it thoroughly tests the interatomic potential, sampling a large number of off-lattice configurations naturally formed on the growth surface when adatoms randomly arrive. In particular, if the potential does not capture the lowest energy for the growth phase relative to other surface configurations, the simulation is likely to result in an incorrect amorphous structure.[54] Second, practical devices often consist of vapor-deposited multilayers of semiconductor compounds, and direct MD simulations of growth reveal defect formation mechanisms and therefore help guide defect control. Finally, previous studies of defects using either *ab initio* or MD methods often assume defect configurations as the initial inputs. In contrast, vapor deposition simulations allow defects to be predicted, thereby eliminating any assumptions about defect configurations.

Vapor deposition simulations were performed to grow all nine of the binary compounds CdTe, CdSe, ZnTe, HgTe, ZnSe, ZnS, HgSe, HgS, and CdS on their zb substrate. Crystalline growth was found for all these compounds. Here, we present two of the most stringent cases. In the first case, a vapor

TABLE IV. Atomic volume Ω (Å^3), cohesive energies E_c (eV/atom), bulk modulus B (eV/Å^3), and elastic constants C' and $C_{44}{}^*$ (eV/Å^3) for the target structures of elements and compounds. Here, C' and $C_{44}{}^*$ are only listed for compound structures. Note that the SW potential predicts similar properties for hcp and fcc, and similar properties for wz and zb (in agreement with experiments and DFT calculations). Note also that asterisk indicates that the calculated $C_{44}{}^*$ values are unrelaxed, which can be much bigger than the experimental values. Relaxed C_{44} is close to the experimental values as will be discussed below.

	Structure		Ω		E_c		B		C'			$C_{44}{}^*$		
Material	Exp.	Model	Exp.[a]	Cal.	Exp.[b]	Cal.	Exp.[c]	Cal.	Exp.[c]	Cal.	Cal.[d]	Exp.[c]	Cal.	Cal.[d]
Zn	hcp	fcc/hcp	16.1	16.1	−1.33	−1.33	0.49	2.60						
Cd	hcp	fcc/hcp	23.1	23.1	−1.13	−1.13	0.39	1.55						
Hg	liquid	fcc	24.6	24.6	−0.61	−0.61	0.16	1.24						
S	orth	fcc	25.7	25.7	−2.85	−2.85	0.13	3.85						
Se	A8	fcc	27.4	27.4	−2.41	−2.41	0.05	2.75						
Te	A8	fcc	34.0	34.0	−2.17	−2.17	0.41	1.88						
ZnS	zb	zb	19.7	19.7	−3.08	−3.08	0.49	0.49	0.12	0.12	0.12	0.29	0.55	0.54
ZnSe	zb	zb	22.8	22.8	−2.69	−2.69	0.39	0.39	0.11	0.14	0.11	0.26	0.45	0.44
ZnTe	zb	zb	28.4	28.4	−2.36	−2.36	0.32	0.32	0.10	0.10	0.09	0.20	0.36	0.36
CdS	wz	zb/wz	24.8	24.8	−2.76	−2.76	0.38	0.38	0.08	0.22	0.08	0.15	0.43	0.40
CdSe	zb	zb	27.7	27.7	−2.52	−2.52	0.33	0.33	0.06	0.16	0.06	0.14	0.37	0.35
CdTe	zb	zb	34.0	34.0	−2.18	−2.18	0.27	0.27	0.05	0.10	0.05	0.13	0.29	0.28
HgS	zb	zb	25.1	25.1	−2.00	−2.00	0.43	0.43	0.06	0.11	0.06	0.17	0.45	0.44
HgSe	zb	zb	28.2	28.2	−1.74	−1.74	0.32	0.32	0.05	0.09	0.05	0.14	0.34	0.33
HgTe	zb	zb	33.7	33.7	−1.55	−1.55	0.26	0.26	0.05	0.07	0.05	0.13	0.28	0.28

[a]From material densities of the equilibrium phases (Ref. 31).
[b]From the equilibrium phases (Ref. 39).
[c]From the equilibrium phases (Refs. 44–48, and 50–53). Experimental elastic constants C' and $C_{44}{}^*$ are only listed for compound structures.
[d]Calculated with modified parameters $\lambda = 5.0$ and γ from r_0 and $u(r_0)$.

deposition simulation was performed to simulate the growth of an alloyed $(Cd_{0.28}Zn_{0.68}Hg_{0.04})(Te_{0.20}Se_{0.18}S_{0.62})$ compound on a ZnS zb substrate. An initial ZnS zb substrate containing 5760 Zn atoms and 6912 S atoms with 48 (101) layers in the x direction, 11 (040) layers in the y direction, and 24 ($\bar{1}01$) layers in the z direction was used. The top y surface was initially terminated by S atoms. The substrate temperature was initially set at $T = 1200$ K by assigning atomic velocities according to a Boltzmann distribution. During simulations, the bottom ($-y$) two (040) layers were held fixed to prevent crystal shift upon adatom impact on the top surface. The next seven (040) layers were isothermally controlled at a desired growth temperature $T = 1200$ K. This left the top two layers free where the motion of atoms was solely determined by Newton's equations of motion. Growth of the alloy was simulated by injecting Cd, Zn, Hg, Te, Se, and S atoms from random locations far above the surface. All adatoms had an initial incident angle $\theta = 0°$ (i.e. the moving direction is perpendicular to the surface), and an initial far-field incident kinetic energy $E_i = 5.0$ eV. Because the SW potential parameters are tailored to the stoichiometric condition, the relative injection frequency of different species was chosen to give a $(Cd_{0.28}Zn_{0.68}Hg_{0.04})(Te_{0.20}Se_{0.18}S_{0.62})$ film composition. The overall adatom injection frequency corresponded to a deposition rate of $R = 0.2$ nm/ns. This deposition rate is much higher than experimental values. However, by maintaining the substrate at an elevated temperature, adatoms have a significant energy to locate low-energy wells on the surface, even within the short time constraint imposed by the high deposition rate. As a result, the effects of accelerated deposition rates on structures were mitigated. To approximately maintain a constant thickness of the free surface region, the isothermal region expanded upward during simulations at about 80% of the surface growth rate. Following the deposition, the system was cooled down from 1200 to 0 K over a 16 ns period. An energy minimization was carried out to further relax the structure. The final configuration obtained is shown in Fig. 2. Figure 2 convincingly verifies that our MD simulation predicts a clean crystalline structure as expected from experiments, even when a variety of randomly disordered configurations involving six different elements are continuously initiated on the surface.

Figure 2 only gives a visual inspection of the structure. We also calculated antisite fractions for the deposited film. We found a very small antisite fraction of 0.0051 for anion (Te, Se, S) atoms to occupy cation (Cd, Zn, Hg) sites, and

TABLE V. Predicted energies per atom (eV) of selected structures for various compounds using modified γ and λ [$\lambda = 5.0$, γ from r_0, $u(r_0)$]. Numbers in bold highlight the lowest energies. Here, zb: zinc-blende; wz: wurtzite; B1: NaCl; B2: CsCl.

Material	zb (target)	wz	B1	B2
ZnS	**−3.080**	−3.080	−2.101	−0.920
ZnSe	**−2.694**	−2.694	−1.863	−0.864
ZnTe	**−2.364**	−2.364	−1.381	−0.522
CdS	−2.763	−2.763	**−2.915**	−2.508
CdSe	−2.523	−2.523	**−2.663**	−2.348
CdTe	**−2.178**	−2.178	−2.157	−1.735
HgS	−2.004	−2.004	**−2.106**	−1.803
HgSe	**−1.738**	−1.738	−1.760	−1.550
HgTe	**−1.554**	−1.554	−1.255	−0.864

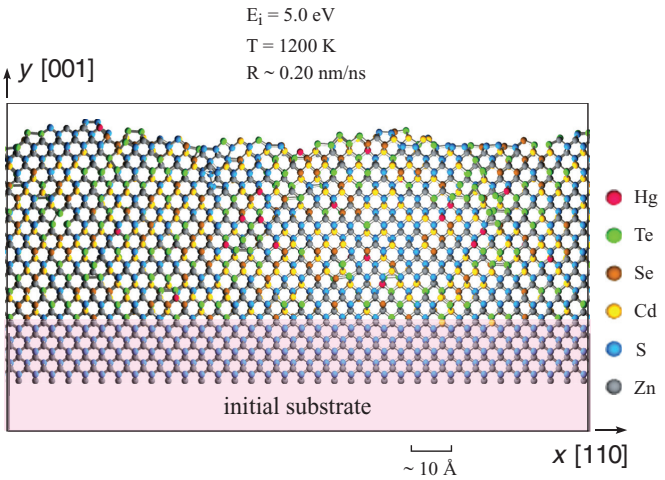

FIG. 2. (Color online) Atomic scale structure of the $(Cd_{0.28}Zn_{0.68}Hg_{0.04})(Te_{0.20}Se_{0.18}S_{0.62})$/ZnS layer obtained from molecular dynamics simulation. The pink shaded area highlights the initial ZnS substrate.

a very small antisite fraction of 0.0003 for cation atoms to occupy anion sites. This verifies that our potential correctly predicts the ordered structure. Furthermore, average radial and bond angle distributions functions over all the 30567 deposited atoms were calculated. The results for the radial and bond angle distributions are shown in Figs. 3(a) and 3(b), respectively, using the solid lines. For comparison, the same radial and bond angle distributions obtained for a perfect zb crystal are shown as the shaded area. It can be seen that the radial distribution peaks of the simulated film align with those of the perfect crystal very well, and the bond angles of the simulated film all center around the tetrahedral angle of 109° as expected for the ideal crystal. These further verify that the predicted film has the zb crystal structure.

In the second case, we demonstrate a vapor deposition simulation that grows HgTe/CdSe/ZnS multilayers. This case is selected for presentation because it is particularly challenging and interesting due to large differences in lattice constants (5.669, 6.050, and 6.460 Å for ZnS, CdSe, and HgTe, respectively) as well as melting temperatures [1991 K (Ref. 55), 1537 K (Ref. 56), and 946 K (Ref. 57) for ZnS, CdSe, and HgTe, respectively]. A large lattice mismatch increases the possibility of misfit dislocations. The propensity of a high density of misfit dislocations and large differences in melting temperatures makes it more difficult to predict the crystalline growth. In fact, we found it necessary to use different growth conditions for different layers in order to minimize defect formation. In addition, the HgTe/CdSe/ZnS multilayers also test all the elements considered in this work.

The same approach and the same ZnS substrate as described above were used in the simulation. Iterative simulations had to be performed in our virtual synthesis to establish the growth conditions for creating high-quality multilayer structures. In particular, different growth temperatures needed to be used to grow each layer. First, approximately 27 Å of ZnS was grown on the initial ZnS substrate at a growth temperature of $T = 1200$ K, using an incident energy of $E_i = 5.0$ eV, and a growth rate of $R \sim 0.42$ nm/ns. Next, about 35 Å of CdSe was grown at a growth temperature of $T = 1100$ K, with an incident energy of $E_i = 5.0$ eV, and a growth rate of $R \sim 0.52$ nm/ns. Finally, about 45 Å of HgTe was grown at a growth temperature of $T = 500$ K, applying an incident energy of $E_i = 0.1$ eV, and a growth rate of $R \sim 0.75$ nm/ns. Following deposition, the same annealing and energy minimization procedure as used above was used to relax the system. The final configuration obtained is shown in Fig. 4.

Figure 4 verifies that our SW potential correctly captures the crystalline growth of the complicated semiconductor multilayer growth. In addition, the formation of a variety of defects is predicted. For example, while the CdSe/ZnS interface is mostly horizontal although contains some steps, the HgTe/CdSe interface and HgTe surface are composed of tilted segments. Misfit dislocations, exhibited as extra half planes about 145° from the y axis in the smaller lattices, are found at both CdSe/ZnS and HgTe/CdSe interfaces. Interestingly, two types of misfit dislocations are observed, one exhibiting only one extra half plane and the other exhibiting two extra half planes. The spacing of these misfit edge dislocations is on the order of 30–40 Å, leading to significant tilting of the (001) growth surface that causes small-angle grain boundaries between neighboring domains (subgrains). Stacking faults are observed in the HgTe layer. Various point defects, such as

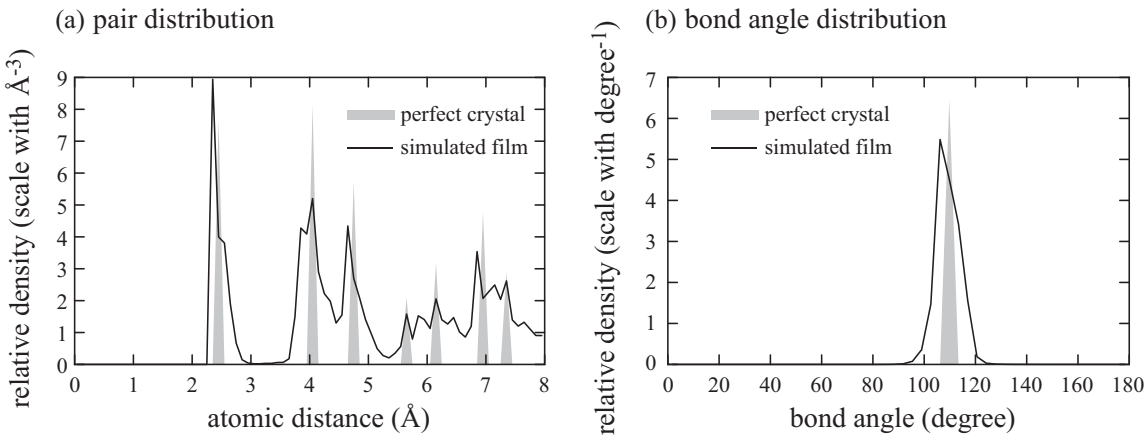

FIG. 3. (a) Radial and (b) bond angle distribution functions obtained from the deposited film shown in Fig. 2.

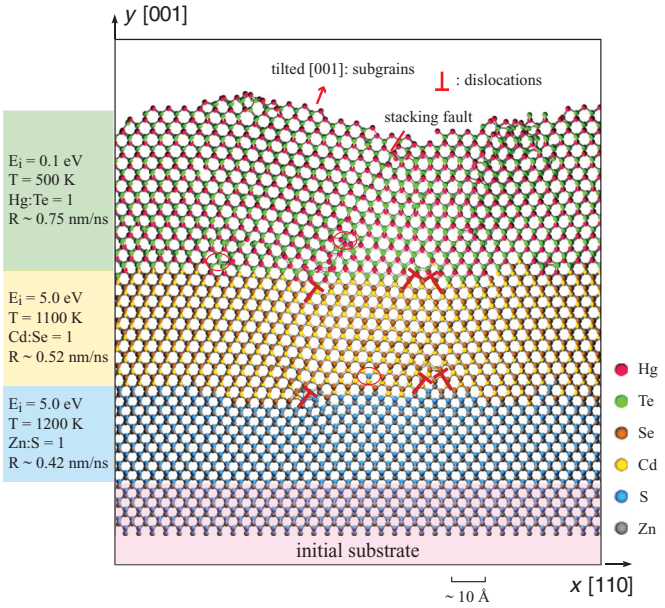

FIG. 4. (Color online) Atomic scale structure of the HgTe/CdSe/ZnS multilayers obtained from molecular dynamics simulation. The pink shaded area highlights the initial ZnS substrate.

antisites, interstitials, and isolated S atoms in the CdSe layer, can also be seen in Fig. 4 (marked by red circles). Although these defects can limit the material properties, they are not easily identifiable in experiments. Our model should provide a powerful means to perform virtual synthesis of the materials in which these defects are reduced through manipulation of growth conditions and design of nanoscale structures. It can also help interpret the phenomena observed with the experimental microscopic methods.

VI. DISCUSSIONS

A. Expanded evaluation of the CdTe case

The results presented above indicate that our Zn-Cd-Hg-S-Se-Te interatomic potential correctly predicts the lowest energy for equilibrium compound structures as compared with any other configurations. It also captures exactly the lattice constants, cohesive energies, and bulk moduli of all compounds. Although representative structures are used to approximate elemental and nonstoichiometric alloyed systems, they do not affect the results under the stoichiometric conditions where these representative structures do not occur. As a result of these, our model can be accurately applied to study defect formation in stoichiometric II-VI semiconductor compounds, even in challenging MD vapor deposition simulations of multilayers. These provide strong verifications about the validity of our SW potential under the stoichiometric conditions. To provide a more complete understanding of our potential, particularly its weaknesses, expanded evaluation was performed using the same methods described previously.[12] In particular, we will compare our model with literature potentials, especially Tersoff and analytical bond order potentials that are capable of capturing nonstoichiometric configurations, including small clusters, various bulk lattices, defects, and

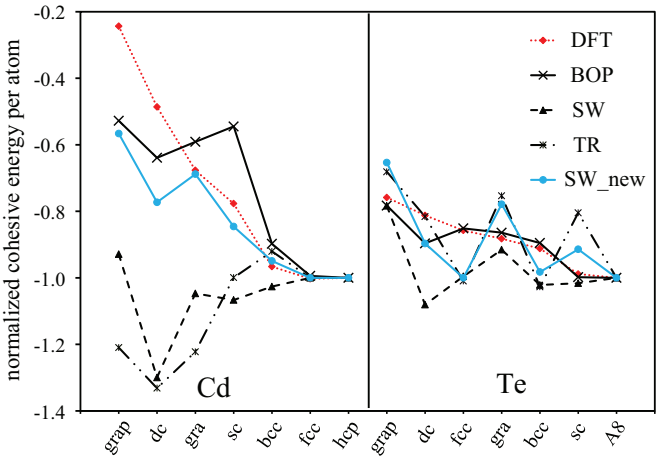

FIG. 5. (Color online) Comparison of cohesive energy for the Cd and Te elemental structures as predicted by DFT, BOP, literature SW, TR, and the new SW presented here (SW_new). Here, grap: graphene; dc: diamond cubic; gra: graphite; sc: simple cubic; bcc: body centered cubic; fcc: face centered cubic; hcp: hexagonal close packed; A8: γ-Se.

surfaces. Such an expanded evaluation for every combination of binary and ternary subsets of the six elements considered here is clearly too exhaustive and is beyond the scope of this paper. Here, we focus only on CdTe system as a case study to provide the understanding of our potential. A similar performance is expected for other subsystems as the potential is developed with a universal parameterization scheme for all the elements.

Several literature CdTe potentials exist for comparison with the new SW potential presented here. These existing potentials with CdTe parameterizations include a different SW (Ref. 25), Tersoff-Rockett[58] (TR), and two BOPs (Refs. 12 and 59). Of the two bond order potentials, the more recent of the two[59] has a more accurate lattice parameter for the CdTe zb lattice and thus will be used. All three literature potentials are compared to our own DFT (Ref. 12) data and experimental values.

As previously stated, capturing the correct lowest energy structure is a basic requirement. Figure 5 compares the normalized (with respect to the experimental lowest energy structure) cohesive energies of several lattice structures for both elements (Cd and Te), where red dashed and blue solid lines refer to DFT and our SW (notated as SW_new) calculations, respectively, the black solid line is from BOP prediction, and the other two (dash and dash-dot-dot) lines are obtained using the literature SW and TR potentials, respectively. It can be seen from Fig. 5 that the energy trends for Cd lattices as predicted by our new SW potential are as close to the DFT result as the BOP. Both our SW and BOP capture the correct hcp phase as the lowest energy Cd structure. They both significantly improve over the literature SW and TR potentials, which incorrectly give a much lower energy for the dc structure than for the hcp structure. Figure 5 also indicates that, although the Te energy trends predicted by our SW are not as close to the DFT results as the BOP, it is comparable or slightly improved over the TR potential (which has bcc as the lowest energy structure) and noticeably better than the literature SW potential (which has again the dc as the lowest energy structure). Note

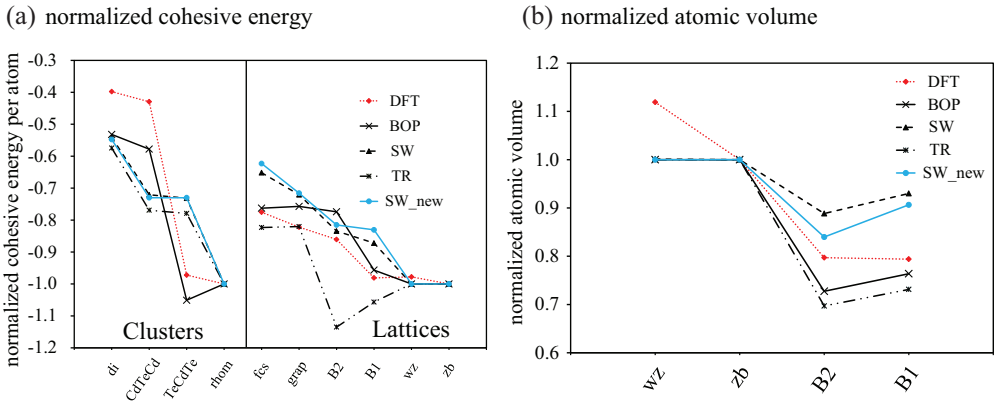

FIG. 6. (Color online) Comparison of (a) cohesive energies for several CdTe clusters and CdTe lattices, and (b) atomic volume for several CdTe lattices as predicted by DFT, BOP, literature SW, TR, and the new SW presented here (SW_new). Here, di: Cd-Te dimer; CdTeCd and TeCdTe: trimers; rhom: CdTeCdTe rhombus; fcs: face centered square; grap: graphene; B2: CsCl; B1: NaCl; wz: wurtzite; zb: diamond cubic.

that, different from the literature SW potential, the energy trends of our SW potential are a result by design, and we could improve the energy trends by using the sc phase as the lowest energy representative structure while increasing the energy for the fcc structure. However, this change is not expected to impact our potential for application under stoichiometric conditions where no elemental phases form.

Figures 6(a) and 6(b) show, respectively, the normalized energies and the normalized atomic volumes for some selected CdTe clusters and lattices. Figure 6(a) indicates that the agreement of the energy trends of our SW potential with the DFT results is comparable with those of the literature SW potential and BOP. The three potentials all captured the lowest energy cluster and lattice correctly. On the other hand, the TR potential incorrectly predicts a $CdTe_2$ trimer and the B2 lattice to have the lowest energy as opposed to the Cd_2Te_2 rhombus cluster and the zb lattice. Not surprisingly, this TR potential does not even allow stable MD simulations of the zb lattice as demonstrated previously.[54] Figure 6(b) shows that the agreement with the DFT atomic volume trends of the selected CdTe lattices is comparable between our SW potential and the literature SW, TR, and BOP potentials. While we do not expect the SW format to reach the same flexibility as the Tersoff and BOP formats on capturing properties of a variety of configurations, the current SW potential does capture exactly the lattice constant of the lowest energy zb lattice. As a result, we believe that it can be accurately applied to address issues related to atomic sizes (e.g., lattice mismatch strain) for the stoichiometric condition where only zb lattices are present.

The relaxed elastic constants and melting temperature for the CdTe zb lattice were calculated. It should be noted that different methods can yield different melting temperatures. Here, we adopted the liquid-solid coexistence method[60] as it is not affected by nucleation of interfaces and has been widely tested to yield reliable melting temperature within the short time MD simulations. Our results of relaxed elastic constants and melting temperatures obtained from different models are compared in Table VI. Note that the melting temperature we obtained for the literature SW potential[25] lies between 1360 and 1390 K. This matches well with ~1370 K obtained from an independent calculation using the same potential[25] [using a direct melting method, however, the same potential yields a different melting temperature of 1305 K (Ref. 61)].

For our new SW potential, it can now be seen from Table VI that, although the unrelaxed elastic constant $C_{44}{}^*$ shown in Table IV is significantly overestimated, the relaxed C_{44} matches the experimental value very well. Overall, the elastic constants and melting temperature predicted by our SW model is comparable to BOP and literature SW potential. In particular, the C_{12} predicted here is closer to the experimental value as compared to the literature SW potential.

TABLE VI. Comparison of elastic constants and melting temperature of CdTe for different interatomic potentials. Here, $C_{44}{}^*$ is unrelaxed.

Property	Exp	DFT	BOP[a]	SW[b]	TR[c]	SW_new
C_{11}(GPa)	53.3[d]	53.2	51.6	44.3	50.7	63.0
C_{12} (GPa)	36.5[d]	36.0	29.2	19.6	37.5	32.0
C_{44} (GPa)	20.4[d]	–	21.0	18.0	15.2	23.6
$C_{44}{}^*$ (GPa)	–	31.8	42.4	30.7	46.8	46.2
T_m (K)	1365[e]	–	1350–1430	1360–1390	700–800	1550–1650

[a]Bond-order potential data (Ref. 59).
[b]Stillinger-Weber data (Ref. 25).
[c]Tersoff-Rockett data (Ref. 58).
[d]Experimental data at 300 K (Ref. 62).
[e]Experimental data (Ref. 63).

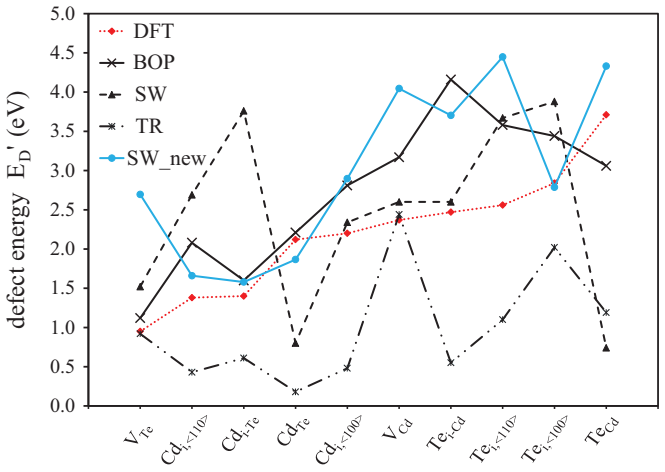

FIG. 7. (Color online) Comparison of intrinsic defect energies as predicted by DFT, BOP, literature SW, TR, and the new SW presented here (SW_new). Here, V_{Te} and V_{Cd}: Te and Cd vacancies, Cd_{Te} and Te_{Cd}: Cd at Te and Te at Cd antisites, $Cd_{i,Te}$ and $Te_{i,Cd}$: Cd interstitial in Te tetrahedron and Te interstitial in Cd tetrahedron, $Cd_{i,\langle 110\rangle}$ and $Te_{i,\langle 110\rangle}$: Cd and Te dumbbell interstitial in the $\langle 110\rangle$ direction, $Cd_{i,\langle 100\rangle}$ and $Te_{i,\langle 100\rangle}$: Cd and Te dumbbell interstitial in the $\langle 100\rangle$ direction.

Energies are calculated for a range of intrinsic defects including vacancies (V_{Te}, V_{Cd}), antisites (Te_{Cd}, Cd_{Te}), single-atom interstitials ($Cd_{i,Te}$, $Te_{i,Cd}$), and dumbbell interstitials ($Te_{i\langle 110\rangle}$, $Te_{i\langle 100\rangle}$, $Cd_{i\langle 110\rangle}$, $Cd_{i\langle 100\rangle}$) as done previously,[12,13] and the results are compared in Fig. 7. It can be seen that the energy trends of the defects predicted by our SW model are fairly similar to those of the DFT and BOP with only two significant differences. First, the V_{Te} is not identified as the low-energy Cd-rich defect. Second, the $Te_{i\langle 100\rangle}$ interstitial is identified as the low-energy Te-rich defect. Again, these may reflect the approximate nature of the SW potential in certain conditions, but also note that there are no sufficient experimental defect energies to validate the models.

Finally, surface energies are calculated. We find the lowest energy surface to be Te-(2×1) under Te-rich conditions and Cd-c(2×2) under Cd-rich conditions. These are to be compared with the BOP predictions of Te-c(2×2) and Cd-(1×2) for Te- and Cd-rich conditions, respectively, and DFT predictions of Cd-(2×1) and Cd-c(2×2) (with coverage of 0.5) for Te- and Cd-rich conditions, respectively.

B. Future improvements of SW potentials

As has been demonstrated in Figs. 2 and 4, a rational parameterization of the SW potential may enable complex growth processes to be correctly simulated, which may promote the application of SW potential in future studies of stoichiometric compounds. There are some limitations of the current SW potential formalism; for example, it cannot capture the elemental structures (e.g., A8 for Se and Te), and the bulk modulus for the fcc structure predicted by the current SW potential formalism is constrained to be above some critical value significantly larger than the real fcc metal (see Table IV). As a result, the present SW potential format may not be applicable for scenarios where elemental domains (such as Se and Te) are present. Here, we provide our perspective as how future SW potentials can be improved based on the insights obtained in this work.

First, the angular function of the conventional SW potentials is essentially a parabolic energy penalty to nontetrahedral bond angles that stabilizes the dc, zb, and wz lattices. However, other angular functions can also be used to stabilize different lattices.[64,65] In one extreme case, an angular function that exhibits multiple minimums can be used to stabilize a variety of lattices.[28,29] Dedicated efforts are needed to pursue this approach.

The SW potential overpredicts the bulk modulus of an fcc structure when either there is a significant angular term (say $\lambda = 32.5$ as assumed in the present work) or there is no angular term ($\lambda = 0$) (Refs. 27 and 66). As discussed in Subsec. II C, this arises because the short cutoff distance of the nearest-neighbor model imposes a minimum curvature of the pair energy at the equilibrium bond length. This problem can be overcome if we replace the pair energy function with one similar to the Tersoff potential[49] where the cutoff distance and energy curvature are independent. In this case, Eqs. (2) and (3) are modified as

$$V_{IJ}^{R}(r) = \frac{E_{b,IJ}\beta_{IJ}}{\beta_{IJ}-\alpha_{IJ}} \exp\left(-\alpha_{IJ}\frac{r-r_{0,IJ}}{r_{0,IJ}}\right) f_{c,IJ}(r), \quad (5)$$

$$V_{IJ}^{A}(r) = \frac{E_{b,IJ}\alpha_{IJ}}{\beta_{IJ}-\alpha_{IJ}} \exp\left(-\beta_{IJ}\frac{r-r_{0,IJ}}{r_{0,IJ}}\right) f_{c,IJ}(r), \quad (6)$$

$$f_{c,IJ}(r) = \begin{cases} 1, & r \leqslant r_{1,IJ} \\ \frac{1}{2}+\frac{1}{2}\cos\left[\frac{\pi(r-r_{1,IJ})}{r_{c,IJ}-r_{1,IJ}}\right], & r_{1,IJ} < r < r_{c,IJ}, \\ 0, & r \geqslant r_{c,IJ} \end{cases} \quad (7)$$

where $r_{0,IJ}$, $E_{b,IJ}$, α_{IJ}, β_{IJ}, $r_{1,IJ}$, and $r_{c,IJ}$ are six pair-dependent parameters, and $f_{c,IJ}(r)$ is a cutoff function. In particular, $r_{c,IJ}$ is cutoff distance, and $r_{1,IJ}$ ($r_{1,IJ} > r_{0,IJ}$) is a starting point to apply the cutoff function. It can be seen from Eqs. (5)–(7) that

$$\frac{d\left[V_{IJ}^{R}(r)-V_{IJ}^{A}(r)\right]}{dr}\Big|_{r=r_{0,IJ}} = 0, \quad (8)$$

$$\left[V_{IJ}^{R}(r)-V_{IJ}^{A}(r)\right]\Big|_{r=r_{0,IJ}} = E_{b,IJ}, \quad (9)$$

$$\frac{d^2\left[V_{IJ}^{R}(r)-V_{IJ}^{A}(r)\right]}{dr^2}\Big|_{r=r_{0,IJ}} = -\frac{E_b\alpha\beta}{r_0^2}. \quad (10)$$

Equations (8) and (9) imply that $r_{0,IJ}$ is the equilibrium bond length, and $E_{b,IJ}$, (< 0) is the equilibrium bond energy. Equation (10) indicates that, when the bond length and bond energy are given, the second derivative of the pair energy can be fitted to any value with additional free parameters α and β. Hence, this pair energy allows the bulk modulus (corresponding to the potential's curvature) to be exactly reproduced.

The ideas described above are easy to implement because they merely change the functions without changing the SW potential format. One way to better capture elemental properties in covalent compound systems is to use hybrid potential formats that combine, for example, the embedded atom method potential for metallic elements with SW potentials for binary interactions.[67] Development of such potentials suitable for a variety of configurations (e.g., those encountered in growth simulations) imposes a research challenge on its own.

C. Conversion between SW and bond order potentials

The SW potential is less transferrable than Tersoff and analytical bond order potentials for nontetrahedral structures. Here, we describe an approach to convert between SW and bond order potentials for configurations that do not significantly deviate from a reference structure. The conversion between SW and Tersoff potentials can be applied similarly.

Considering only the σ bond interaction, the bond order potential[12–18] can be expressed as

$$E = \frac{1}{2}\sum_{i=1}^{N}\sum_{j=i_1}^{i_N}[\phi_{IJ}(r_{ij}) - 2\Theta_{ij}\beta_{\sigma,IJ}(r_{ij})], \tag{11}$$

where $\phi_{IJ}(r)$ is a pairwise repulsive function, $\beta_{\sigma,IJ}(r)$ is a pairwise σ bond integral function, and Θ_{ij} is the bond order between i and j. The bond order is expressed as:

$$\Theta = \frac{1}{\sqrt{1 + c_{\sigma,IJ}\Phi^i + c_{\sigma,IJ}\Phi^j}}, \tag{12}$$

where $c_{\sigma,IJ}$ is a parameter, and Φ^i and Φ^j are local environment dependent variables expressed as

$$\Phi^i = \sum_{\substack{k=i_1\\k\neq j}}^{i_N} g^2_{\sigma,JIK}(\theta_{jik})\left[\frac{\beta_{\sigma,IK}(r_{ik})}{\beta_{\sigma,IJ}(r_{ij})}\right]^2, \tag{13}$$

$$\Phi^j = \sum_{\substack{k=j_1\\k\neq i}}^{j_N} g^2_{\sigma,IJK}(\theta_{ijk})\left[\frac{\beta_{\sigma,JK}(r_{jk})}{\beta_{\sigma,IJ}(r_{ij})}\right]^2. \tag{14}$$

For a simple reference bulk crystal, symmetry leads to $\Phi^i = \Phi^j$. Assume that, for this reference structure, $\Phi^i = \Phi^j = \Phi^0$, we can write

$$\begin{aligned}\Theta &= \frac{1}{\sqrt{1 + 2c_{\sigma,IJ}\Phi^0 + (2c_{\sigma,IJ}\Phi^i - 2c_\sigma\Phi^0)}}\\ &= \frac{1}{\sqrt{1+2c_{\sigma,IJ}\Phi^0}\sqrt{1+\left(\frac{2c_{\sigma,IJ}\Phi^i - 2c_{\sigma,IJ}\Phi^0}{1+2c_{\sigma,IJ}\Phi^0}\right)}} \approx \frac{1}{\sqrt{1+2c_{\sigma,IJ}\Phi^0}}\left[1 - \frac{1}{2}\left(\frac{2c_{\sigma,IJ}\Phi^i - 2c_{\sigma,IJ}\Phi^0}{1+2c_{\sigma,IJ}\Phi^0}\right)\right]\\ &= \frac{1}{\sqrt{1+2c_{\sigma,IJ}\Phi^0}}\frac{1+3c_{\sigma,IJ}\Phi^0}{1+2c_{\sigma,IJ}\Phi^0} - \frac{1}{\sqrt{1+2c_{\sigma,IJ}\Phi^0}}\frac{c_{\sigma,IJ}\Phi^i}{1+2c_{\sigma,IJ}\Phi^0}.\end{aligned} \tag{15}$$

As a result, Eq. (11) becomes:

$$\begin{aligned}E &= \frac{1}{2}\sum_{i=1}^{N}\sum_{j=i_1}^{i_N}[\phi_{IJ}(r_{ij}) - 2\Theta_{ij}\beta_{\sigma,IJ}(r_{ij})]\\ &= \frac{1}{2}\sum_{i=1}^{N}\sum_{j=i_1}^{i_N}\left[\phi_{IJ}(r_{ij}) - \frac{2}{\sqrt{1+2c_{\sigma,IJ}\Phi^0}}\frac{1+3c_{\sigma,IJ}\Phi^0}{1+2c_{\sigma,IJ}\Phi^0}\beta_{\sigma,IJ}(r_{ij}) + \frac{1}{\sqrt{1+2c_{\sigma,IJ}\Phi^0}}\frac{2c_{\sigma,IJ}\Phi^i}{1+2c_{\sigma,IJ}\Phi^0}\beta_{\sigma,IJ}(r_{ij})\right]\\ &= \frac{1}{2}\sum_{i=1}^{N}\sum_{j=i_1}^{i_N}\left\{\phi_{IJ}(r_{ij}) - \frac{2}{\sqrt{1+2c_{\sigma,IJ}\Phi^0}}\frac{1+3c_{\sigma,IJ}\Phi^0}{1+2c_{\sigma,IJ}\Phi^0}\beta_{\sigma,IJ}(r_{ij})\right.\\ &\quad\left. + \frac{1}{\sqrt{1+2c_{\sigma,IJ}\Phi^0}}\frac{2c_{\sigma,IJ}}{1+2c_{\sigma,IJ}\Phi^0}\beta_{\sigma,IJ}(r_{ij})\sum_{\substack{k=i_1\\k\neq j}}^{i_N} g^2_{\sigma,JIK}(\theta_{jik})\left[\frac{\beta_{\sigma,IK}(r_{ik})}{\beta_{\sigma,IJ}(r_{ij})}\right]^2\right\}.\end{aligned} \tag{16}$$

Note that for the nearest neighbor model with an ideal bulk crystal, $\beta_{\sigma,IK}(r_{ik}) = \beta_{\sigma,IJ}(r_{ij})$. Equations (1) and (16) can be made equivalent for any configurations that are not significantly deviated from the reference structure if we set:

$$g^2_{\sigma,JIK}(\theta_{jik}) = \left(\cos\theta_{jik} + \frac{1}{3}\right)^2, \tag{17}$$

$$\beta_{\sigma,IJ}(r_{ij}) = k[u_{IJ}(r_{ij})]^2, \tag{18}$$

$$\frac{1}{\sqrt{1+2c_{\sigma,IJ}\Phi^0}}\frac{2c_{\sigma,IJ}}{1+2c_{\sigma,IJ}\Phi^0}k = 1, \tag{19}$$

$$\begin{aligned}\phi_{IJ}(r_{ij}) &= V^R_{IJ}(r_{ij}) - V^A_{IJ}(r_{ij})\\ &\quad + \frac{2}{\sqrt{1+2c_{\sigma,IJ}\Phi^0}}\frac{1+3c_{\sigma,IJ}\Phi^0}{1+2c_{\sigma,IJ}\Phi^0}k[u_{IJ}(r_{ij})]^2\\ &= V^R_{IJ}(r_{ij}) - V^A_{IJ}(r_{ij}) + \frac{1+3c_{\sigma,IJ}\Phi^0}{c_{\sigma,IJ}}[u_{IJ}(r_{ij})]^2.\end{aligned} \tag{20}$$

Here, we introduce an adjustable number k to ensure that Eqs. (17)–(20) are all satisfied.

We have used this approach to convert the Zn-Cd-Hg-S-Se-Te SW potential to bond order potential using dz elemental and zb compound crystals as the reference structures. We found that with an appropriate parameter of $k = 10$, the converted bond order potential maintains the relative energy trends between elements, nonstoichiometric alloys, and compounds. It also reproduces exactly the lattice constants, cohesive energies, and elastic constants of all the stoichiometric compounds. As a result, the converted BOP also predicts the crystalline growth for all the compounds.

VII. CONCLUSIONS

This work explores several insights about the SW potentials not discussed previously. First, the SW potential can be constructed to serve as a good model for semiconductor compound simulations under stoichiometric conditions. This can be achieved by incorporating the correct energy trends to prevent the system from evolving towards nonstoichiometric structures and by capturing exactly the characteristic properties of stoichiometric compounds. We found that all the potential parameters (including the cutoff distance) need to be optimized in order to exactly match the lattice constants, cohesive energies, bulk moduli, and shear elastic constants C' of the compounds. Although in general C_{44} is insensitive to the SW potential parameters, our calculations of the relaxed C_{44} value for the zb CdTe structure end up close to the experimental measurement. Our analysis also identifies additional user flexibility to select parameters λ and γ in order to adapt to their needs to ensure the lowest energy for the equilibrium compound phase as well as to accurately predict the shear elastic constant C'. Methods that could further enhance the use of future SW potentials in other contexts are also proposed.

Our Zn-Cd-Hg-S-Se-Te Stillinger-Weber potential was parameterized according to these insights. The results are encouraging: the model accurately reproduces the cohesive energies, lattice constants, and bulk moduli of all binary compounds while also ensuring the correct transformation between elements, nonstoichiometric alloys, and stoichiometric compounds. Consequently, the potential correctly predicts the crystalline growth of all stoichiometric compounds during molecular dynamics simulation of vapor deposition under stoichiometric growth conditions. Most importantly, we demonstrate two successful growth simulations. In the first case, the crystalline growth of an alloyed $(Cd_{0.28}Zn_{0.68}Hg_{0.04})(Te_{0.20}Se_{0.18}S_{0.62})$ compound on a ZnS substrate is predicted from a MD simulation, convincingly verifying that our model predicts the correct structure evolution from any of the random configurations involving any of the combinations of the six elements. In the second case, we demonstrate the predictive power of our model on defects such as misfit dislocations, stacking faults, and subgrain nucleation using a MD simulation of vapor deposition of a complex HgTe/CdSe/ZnS multilayer system. This indicates that our model provides a powerful means to study defect formation in II-VI semiconductor compounds, avoiding *a priori* assumptions about defect configurations.

ACKNOWLEDGMENTS

Sandia National Laboratories is a multiprogram laboratory managed and operated by Sandia Corporation, a wholly owned subsidiary of Lockheed Martin Corporation, for the US Department of Energy's National Nuclear Security Administration under Contract No. DE-AC04-94AL85000. This work was performed under DOE Project No. EE0005859-2013Q3, and under a Laboratory Directed Research and Development (LDRD) project.

*Email address: xzhou@sandia.gov

[1] A. Rogalski, Rep. Prog. Phys. **68**, 2267 (2005).
[2] W. E. Tennant, C. A. Cockrum, J. B. Gilpin, M. A. Kinch, M. B. Reine, and R. P. Ruth, J. Vac. Sci. Technol. B **10**, 1359 (1992).
[3] T. E. Schlesinger, J. E. Toney, H. Yoon, E. Y. Lee, B. A. Brunett, L. Franks, and R. B. James, Mater. Sci. Eng. **32**, 103 (2001).
[4] P. J. Sellin, Nucl. Instrum. Methods Phys. Res., Sect. A **513**, 332 (2003).
[5] A. Peurrung, Mater. Today **11**, 50 (2008).
[6] T. Takahashi and S. Watanabe, IEEE Trans. Nucl. Sci. **48**, 950 (2001).
[7] K. Zweibel, Science **328**, 699 (2010).
[8] P. T. K. Chin, C. de M. Donega, S. S. van Bavel, S. C. J. Meskers, N. A. J. M. Sommerdijk, and R. A. J. Janssen, J. Am. Chem. Soc. **129**, 14880 (2007).
[9] N. M. Haegel, S. E. Williams, C. L. Frenzen, and C. Scandrett, Semicond. Sci. Technol. **25**, 055017 (2010).
[10] V. Babentsov, V. Boiko, G. A. Schepelskii, R. B. James, J. Franc, J. Prochazka, and P. Hlidek, Nucl. Instrum. Methods Phys. Res., Sect. A **633**, S81 (2011).
[11] D. Zeng, W. Jie, T. Wang, G. Zha, and J. Zhang, Nucl. Instrum. Methods Phys. Res., Sect. A **586**, 439 (2008).
[12] D. K. Ward, X. W. Zhou, B. M. Wong, F. P. Doty, and J. A. Zimmerman, Phys. Rev. B **85**, 115206 (2012).
[13] D. K. Ward, X. W. Zhou, B. M. Wong, F. P. Doty, and J. A. Zimmerman, Phys. Rev. B **86**, 245203 (2012).
[14] D. G. Pettifor, M. W. Finnis, D. Nguyen-Manh, D. A. Murdick, X. W. Zhou, and H. N. G. Wadley, Mater. Sci. Eng. A **365**, 2 (2004).
[15] D. G. Pettifor and I. I. Oleinik, Phys. Rev. Lett. **84**, 4124 (2000).
[16] D. G. Pettifor and I. I. Oleinik, Phys. Rev. B **65**, 172103 (2002).
[17] D. G. Pettifor and I. I. Oleinik, Phys. Rev. B **59**, 8487 (1999).
[18] R. Drautz, D. A. Murdick, D. Nguyen-Manh, X. W. Zhou, H. N. G. Wadley, and D. G. Pettifor, Phys. Rev. B **72**, 144105 (2005).
[19] J. Tersoff, Phys. Rev. B **37**, 6991 (1988).
[20] X. W. Zhou, D. K. Ward, B. M. Wong, F. P. Doty, J. A. Zimmerman, G. N. Nielson, J. L. Cruz-Campa, V. P. Gupta, J. E. Granata, J. J. Chavez, and D. Zubia, Phys. Rev. B **85**, 245302 (2012).
[21] F. H. Stillinger and T. A. Weber, Phys. Rev. B **31**, 5262 (1985).
[22] C. H. Grein, J. P. Faurie, V. Bousquet, E. Tournie, R. Benedek, and T. de la Rubia, J. Cryst. Growth **178**, 258 (1997).
[23] M. Ichimura, Phys. Status Solidi A **153**, 431 (1996).

[24]Z. Zhang, A. Chatterjee, C. Grein, A. J. Ciani, and P. E. Chung, J. Electron. Mater. **40**, 109 (2011).
[25]Z. Q. Wang, D. Stroud, and A. J. Markworth, Phys. Rev. B **40**, 3129 (1989).
[26]S. Wacke, T. Gorecki, C. Gorecki, and K. Ksiazek, 15th Inter. Semi. Phys. Chem. Sol., J. Phys. Conf. Ser. **289**, 012020 (2011).
[27]X. W. Zhou, R. E. Jones, C. J. Kimmer, J. C. Duda, and P. E. Hopkins, Phys. Rev. B **87**, 094303 (2013).
[28]X. W. Zhou and H. N. G. Wadley, Comput. Mater. Sci. **39**, 340 (2007).
[29]X. W. Zhou and H. N. G. Wadley, Comput. Mater. Sci. **39**, 541 (2007).
[30]X. W. Zhou and R. E. Jones, Modell. Simul. Mater. Sci. Eng. **19**, 025004 (2011).
[31]J. D. H. Donnay and H. M. Ondik, *Crystal Data, Determinative Tables*, 3rd ed., Vol. 2 (inorganic compounds) (US Department of Commerce, National Bureau of Standards, and Joint Committee on Power Diffraction Standards, USA, 1973).
[32]A. Bere and A. Serra, Phys. Rev. B **65**, 205323 (2002).
[33]A. Bere and A. Serra, Philos. Mag. **86**, 2159 (2006).
[34]C.-Y. Yeh, W. Lu, S. Froyen, and A. Zunger, Phys. Rev. B **46**, 10086 (1992).
[35]A. W. Vere, S. Cole, and D. J. Williams, J. Electron. Mater. **12**, 551 (1983).
[36]M. Winkler, M. Schenk, and I. Hahnert, Cryst. Res. Technol. **27**, 1047 (1992).
[37]L. V. Woodcock, Nature **385**, 141 (1997).
[38]G. Jackson and F. van Swol, Mol. Phys. **65**, 161 (1988).
[39]I. Barin, O. Knacke, and O. Kubaschewski, *Thermochemical Properties of Inorganic Compounds* (Springer-Verlag, Berlin, 1977).
[40]M. I. Baskes, Phys. Rev. B **46**, 2727 (1992).
[41]Z. Q. Wang and D. Stroud, Phys. Rev. B **42**, 5353 (1990).
[42]J. Kioseoglou, H. M. Polatoglou, L. Lymperakis, G. Nouet, and Ph. Komninou,Comput. Mater. Sci. **27**, 43 (2003).
[43]H. Koizumi, Y. Kamimura, and T. Suzuki, Philos. Mag. A **80**, 609 (2000).
[44]B. Derby, Phys. Rev. B **76**, 054126 (2007).
[45]G. Mistra, P. Tripathi, and S. C. Goyal, Philos. Mag. Lett. **87**, 393 (2007).
[46]J. E. Ayers, *Heteroepitaxy of Semiconductors Theory, Growth, and Characterization* (CRC Press, Boca Raton, 2007).
[47]O. Madelung, M. Schulz, H. Weiss, Landolt-Borstein (Eds.), *Numerical Data and Functional Relationships in Science and Technology*, Vol. 17 (Springer, Berlin, 1982).
[48]F. Bechstedt and W.A. Harrison, Phys. Rev. B **39**, 5041 (1989).
[49]J. Tersoff, Phys. Rev. B **39**, 5566 (1989).
[50]C. W. Garland and R. Dalven, Phys. Rev. **111**, 1232 (1958).
[51]C. W. Garland and J. Silverman, Phys. Rev. **119**, 1218 (1960).
[52]C. F. Cline, H. L. Dunegan, and G. W. Henderson, J. Appl. Phys. **38**, 1944 (1967).
[53]http://www.periodictable.com/Properties/A/BulkModulus.html.
[54]D. K. Ward, X. W. Zhou, B. M. Wong, F. P. Doty, and J. A. Zimmerman, J. Chem. Phys. **134**, 244703 (2011).
[55]R. C. Sharma and Y. A. Chang, J. Phase Equilib. **17**, 261 (1996).
[56]R. C. Sharma and Y. A. Chang, J. Phase Equilib. **17**, 140 (1996).
[57]R. C. Sharma, Y. A. Chang, and C. Guminski, J. Phase Equilib. **16**, 338 (1995).
[58]J. Oh and C. H. Grein, J. Cryst. Growth **193**, 241 (1998).
[59]D. K. Ward, X. W. Zhou, B. M. Wong, and F. P. Doty (unpublished).
[60]J. R. Morris, C. Z. Wang, K. M. Ho, and C. T. Chan, Phys. Rev. B **49**, 3109 (1994).
[61]C. Henager, Jr. and J. R. Morris, Phys. Rev. B **80**, 245309 (2009).
[62]J. M. Rowe, R. M. Nicklow, D. L. Price, and K. Zanio, Phys. Rev. B **10**, 671 (1974).
[63]I. S. Grigoriev and E.Z. Meilikhov, *Handbook of Physical Quantities* (CRC Press, New York, 1997).
[64]R. W. J. M. Huang, F. Chung, and S. W. de Leeuw, Solid State Ionics **175**, 851 (2004).
[65]J. V. L. Beckers, K. J. van der Bent, and S. W. de Leeuw, Solid State Ionics **133**, 217 (2000).
[66]X. W. Zhou, Reese E. Jones, J. C. Duda, and P. E. Hopkins, Phys. Chem. Chem. Phys. **15**, 11078 (2013).
[67]A. M Dongare, B. LaMattina, D. L Irving, A. M. Rajendran, M. A. Zikry, and D. W. Brenner, Modell. Simul. Mater. Sci. Eng. **20**, 035007 (2012).